



# Enhanced visible light-driven photocatalytic performance of Zr doped CeO<sub>2</sub> nanoparticles

M. A. Majeed Khan<sup>1</sup> · Wasi Khan<sup>2</sup> · M. Naziruddin Khan<sup>1</sup> · Abdulaziz N. Alhazaa<sup>1,3</sup>

Received: 21 November 2018 / Accepted: 13 March 2019 / Published online: 26 March 2019  
© Springer Science+Business Media, LLC, part of Springer Nature 2019

## Abstract

In this study, pristine and Zr-doped CeO<sub>2</sub> nanoparticles with chemical formula Ce<sub>1-x</sub>Zr<sub>x</sub>O<sub>2</sub> (x = 0, 0.05, 0.075 and 0.1) have been prepared through facile hydrothermal process. The influence of Zr doping on the microstructure, thermal, optical and photocatalytic properties of CeO<sub>2</sub> was systematically explored through various analytical techniques. Analysis of the XRD data reveals cubic fluorite structure of the samples with average crystallite size of 12, 15, 21 and 30 nm respectively for different Zr doping. The optical properties of the nanoparticles were studied through UV–visible absorption and photoluminescence (PL) spectroscopy. X-ray photoelectron spectroscopy (XPS) and Raman spectroscopy measurements were performed to examine the chemical state and microstructure of the synthesized materials. The functional groups and mode of vibrations have been identified by the Fourier transform infrared (FTIR) spectroscopy. A reduction in the optical band gap of CeO<sub>2</sub> (from 3.25 to 3.10 eV) is observed on systematic Zr doping. In addition, significant enhancement in the photocatalytic performance is also noticed for the doped samples (92.2%) as compared to the pristine one (68.7%) for the degradation of methylene blue (MB) dye under visible light irradiation.

## 1 Introduction

In recent years, nanostructure semiconductors have attracted much interest owing to their novel features different from their bulk counterpart [1]. These innovative characteristics of nanomaterials may find promising applications in photoelectronics, catalysis, optics, magnetic devices etc. [2–8]. Among the various semiconductors, ceria oxide (CeO<sub>2</sub>) is one of the important rare earth oxides due to its exceptional technological applications in solar cells [9], solid oxide fuel cell electrolyte materials [10], oxygen storage capacity [11], catalysts [12], oxygen storage materials, optoelectronic and electrochemical devices [13]. Moreover, it is known that CeO<sub>2</sub> is very reactive, strong oxidizing agent and has wide band gap with different morphologies, that are utilized as photocatalyst in environmental purification,

three-way catalysts for the elimination of toxic auto-exhaust gases, oxygen permeation membrane systems, UV blockers, biological applications [14–20]. However, it may worth to mention few disadvantage of catalysts in operating for different processes under different temperature as compared to the other catalysts. In fact, firstly, the temperature inside the catalytic reactor needs to be initially low in order to allow the adsorption of the pollutants onto the porous substrate at high temperatures, and then the pollutants will be released from the porous substrate. Secondly, the temperature needs to increase to allow the oxidation of the pollutants and to regenerate the adsorptive property of the porous substrate. The limit of adsorption and the competitive effect of the involved pollutants need to be carefully investigated in order to avoid their release into the environment. It is reported that the band gap and other essential properties of nanoscale CeO<sub>2</sub> can be considerably modified by the doping of suitable dopants associated with the formation of defect states between valence band and conduction band, i.e. red shift of UV spectra [21]. In order to improve its catalytic performance, zirconium has been widely used to form Ce–Zr solid solution [22]. The oxidative performance of ceria-based catalysts is closely related to the oxygen vacancies and species. Hori et al. [23] have reported three to five times higher oxygen storage capacity due to zirconium doping in CeO<sub>2</sub>.

✉ M. A. Majeed Khan  
majeed\_phys@rediffmail.com

<sup>1</sup> King Abdullah Institute for Nanotechnology, King Saud University, 11451 Riyadh, Saudi Arabia

<sup>2</sup> Department of Physics, Aligarh Muslim University, 202002 Aligarh, India

<sup>3</sup> Physics and Astronomy Department, King Saud University, Riyadh 11451, Saudi Arabia

However improved thermal resistance and redox properties of Zr doped ceria were observed by Adamowska et al. [24]. But, there is always a chance to improve the properties of existing material by various means and hence doping is one of the important routes in order to achieve new and better properties of nanostructure materials. In this context, substitution of Zr to form  $Ce_{1-x}Zr_xO_2$  matrix alters the structural and electronic properties of  $CeO_2$ . This enhances the chemical and thermal stability of the system than the pristine ceria [25–27]. A significant modification is also observed in the optical properties of doped  $CeO_2$ , attributed to the transition of electrons between O 2p and the lower unoccupied energy level of the dopants. Moreover, enhancement in the degradation of organic pollutants will surely influence our environment that will be beneficial for human health. Several physical and chemical methods have been developed for the synthesis of  $CeO_2$  doped with different concentrations of  $Zr^{4+}$  ions, such as sol–gel [28], co-precipitation [29], hydrothermal processes [30], modified co-precipitation, flame pyrolysis [31] etc. Among all the methods, we have tried hydrothermal approach to synthesize pristine and Zr-doped  $CeO_2$  nanostructures. The prepared samples were characterized by various analytical techniques to investigate the influence of Zr doping on the physico-chemical properties of  $CeO_2$ .

## 2 Experimental details

Nanoparticles of  $Ce_{1-x}Zr_xO_2$  ( $x = 0, 0.05, 0.075$  and  $0.1$ ) were synthesized via a simple hydrothermal process by varying the amounts of reactants. AR grade cerium and zirconium nitrates were used without purification. Typically, 5 mmol of cerium nitrate and 0.25 (5%), 0.375 (7.5%) and 0.50 (10%) mmol of zirconium nitrate were dissolved in 20 ml distilled water and kept on a magnetic stirrer until the salts completely dissolved. The pH value was adjusted to 7 by the addition of 0.1 M solution of NaOH during this reaction. Thereafter, product was placed in an autoclave with 100 ml polytetrafluoroethylene liner at 100 °C for 24 h. The obtained white precipitate was carefully washed with distilled water and ethanol to eliminate organic impurities. Then the precipitate was dried at 80 °C overnight followed by the calcination at 500 °C for 5 h in a muffle furnace to get nanoparticles of  $CeO_2$  and Zr doped  $CeO_2$  as final product.

The prepared samples were characterized using different analytical techniques. An XRD system (PANalytical, X'Pert High) having  $CuK_{\alpha}$  radiation ( $\lambda = 1.5406 \text{ \AA}$ ) was used to determine the crystal structure and phase purity of the samples in the  $2\theta$  range of  $10^{\circ}$ – $100^{\circ}$  at a scanning speed of  $2^{\circ}/\text{min}$ . The X-ray photoelectron spectroscopy (XPS) measurements were performed with monochromatic Mg  $K_{\alpha}$  line (1253.6 eV) radiation source on an ESCA model VG

3000 system. Field emission scanning electron microscope (FE-SEM) was used to observe surface morphology of the samples. The Fourier transform infrared (FTIR) spectra were registered on PerkinElmer FTIR spectrometer in the wavenumbers  $400$ – $4000 \text{ cm}^{-1}$ . The micro-Raman and PL spectra were recorded at room temperature using Horiba Raman/PL system (IY-Horiba-T64000) having a continuous wave laser operating at a 325 nm. The optical properties were studied through UV–visible spectrophotometer (Shimadzu-2550, Japan) in the wavelength range of 300–900 nm. The photocatalytic degradation of  $Ce_{1-x}Zr_xO_2$  ( $x = 0, 0.05, 0.075$  and  $0.1$ ) nanoparticles was examined by the degradation of methylene blue (MB) organic dye in an aqueous solution under visible light irradiation produced by the 400 W Xenon lamp ( $\lambda \sim 400 \text{ nm}$ ). In a typical experiment, 50 mg undoped and doped samples were added to 100 ml solution (10 mg/L) of the MB dye and then stirred on a magnetic stir in the dark environment for 1 h to found adsorption/desorption equilibrium between the reactants and catalysts. The light source was placed above the samples in order to irradiate them in the normal direction. The distance between the samples and the light source was kept about 20 cm. During the process of the reaction, about 2 ml suspensions were taken and centrifuged and then filtered to remove the residual catalyst particulates for analysis. Thereafter, the change in MB concentration was monitored using Shimadzu UV-1800 spectrometer at a wavelength of 664 nm.

The degradation efficiency ( $\eta$ ) of MB dye was evaluated by the following equation:

$$\eta = \left( 1 - \frac{C}{C_0} \right) \times 100$$

where  $C_0$  gives the initial concentration of the solution and  $C$  is the concentration after light irradiation.

## 3 Results and discussion

### 3.1 XRD

Phase purity and crystal structure of the prepared samples were examined through XRD patterns recorded at room temperature. These patterns for undoped and Zr doped  $CeO_2$  samples are shown in Fig. 1. All diffractograms contain ten main Bragg's peaks that correspond to the (111), (200), (220), (311), (222), (400), (331), (420), (422) and (333) planes, located at angles ( $2\theta$ )  $\sim 28.93, 33.44, 47.85, 56.74, 59.33, 69.67, 77.11, 79.37, 88.77$  and  $95.87^{\circ}$  respectively. These peaks are well matched with the cubic fluorite-type phase of pure  $CeO_2$  having  $Fm\bar{3}m$  space group (JCPDS no 34-0394) and unit cell parameter,  $a = 5.41 \text{ \AA}$ . No any additional peak corresponding to Zr related impurity phases was

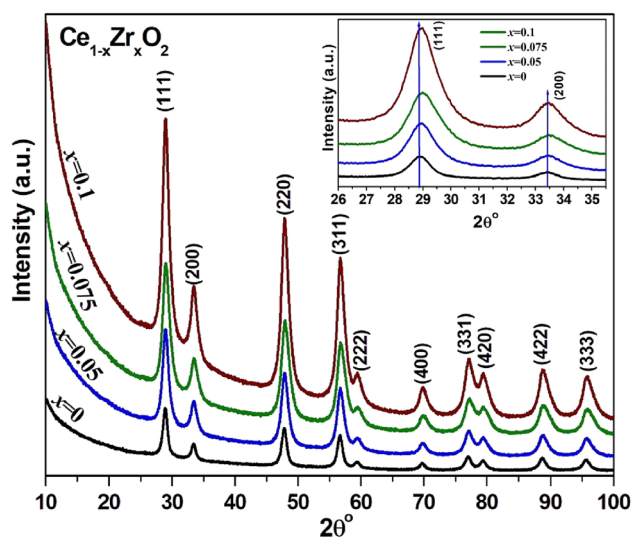


**Fig. 1** XRD patterns of  $\text{Ce}_{1-x}\text{Zr}_x\text{O}_2$  ( $x=0, 0.05, 0.075$  and  $0.1$ ) samples. Inset shows a shift in the (111) plane of  $\text{CeO}_2$

**Table 1** Crystallite size, lattice constant and optical band gap of undoped and Zr-doped  $\text{CeO}_2$  nanoparticles

Zr conc. ( $x$ )	Crystallite size from Scherrer eq. (nm)	Lattice constant (Å)	Optical band gap (eV)
0	$12 \pm 1.6$	5.411	3.25
0.05	$15 \pm 1.4$	5.413	3.16
0.075	$21 \pm 1.2$	5.420	3.12
0.1	$30 \pm 1.1$	5.397	3.10

detected that confirms high purity and single phase of the samples.

The lattice parameters ( $a=b=c$ ) of the undoped and Zr doped  $\text{CeO}_2$  nanostructures are estimated from the XRD patterns using the following equation [32]:

$$\frac{1}{d_{hkl}^2} = \frac{h^2 + k^2 + l^2}{a^2}$$

where  $d_{hkl}$  is the interplanar spacing. The calculated values of the lattice parameters are given in Table 1. It is clear that the lattice parameter slightly varies by the doping of Zr ions in pristine  $\text{CeO}_2$  [32]. For the undoped sample, its value is very close to the theoretical result ( $a=5.41 \text{ \AA}$ ) that indicates possible replacement of Ce by the Zr ions in the cubic fluorite structure. Additionally, it is evident from the XRD patterns that the most intense diffraction peak (111) in Zr doped  $\text{CeO}_2$  slightly shift towards the higher angles (inset Fig. 1) that signifies that the Zr substitution affects/distort the crystal structure of the samples. This may be due to the difference in the ionic radii of zirconium and cerium ions.

The average crystallite size ( $t$ ) is evaluated using the full width at half maximum (FWHM) of the most intense (111) peak by the Scherrer's equation given as [33]:

$$t = \frac{k\lambda}{\beta \cos \theta}$$

where  $k$  is a constant equal to 0.94,  $\beta$  and  $\theta$  are the FWHM and position of the most intense peak respectively. The obtained values of the crystallite size for undoped and Zr doped  $\text{CeO}_2$  NPs are given in Table 1.

### 3.2 XPS analysis

The surface composition and chemical states of  $\text{Ce}_{1-x}\text{Zr}_x\text{O}_2$  samples were investigated through XPS measurements. Figure 2a shows a typical XPS survey spectrum of  $\text{Ce}_{0.95}\text{Zr}_{0.05}\text{O}_2$  sample. The core levels of Ce 3d, Ce 4p, Zr 3d, and O 1s have been classified in the spectrum. In the spectrum of Ce 3d, six peaks are observed and shown in Fig. 2b. Out of these, peaks appeared at 881.29, 888.10, and 897.9 eV assigned to the Ce  $3d_{5/2}$  components, whereas remaining signals of Ce  $3d_{3/2}$  could be seen at 906.1, and 915.8 eV. Two main peaks of Zr 3d are noticed at 181.6 and 183.9 eV associated with Zr  $3d_{5/2}$  and Zr  $3d_{3/2}$  respectively (Fig. 2c). This indicates 4+ oxidation state of Zr in  $\text{Ce}_{1-x}\text{Zr}_x\text{O}_2$  matrix and in good agreement with the earlier reported work [34–36]. The O 1s XPS spectra show significant changes on Zr incorporation which is very clear in Fig. 2d and further revealed a notable shift in the XPS peak towards lower binding energy as compared to the pristine  $\text{CeO}_2$ . The main peak is appeared at 531.26 eV attributed to the presence of oxygen atoms [37–39], while another peak obtained at 528.10 eV may be due to the chemisorption of oxygen caused by surface hydroxyl associated with the O–H bonds [40, 41].

### 3.3 SEM/HRTEM

In order to obtain more detailed information about the internal structure of the synthesized samples, electron microscopy measurements were carried out using FESEM/HRTEM and images are displayed in Fig. 3. The FESEM micrographs of pristine and 10% Zr doped  $\text{CeO}_2$  samples shown in Fig. 3a, b exhibit spherical shape and agglomeration of the nanoparticles in both the samples. It is also evident that the particles size increases in the doped sample which is consistent with the XRD results. Figure 3c, d shows HRTEM micrographs of the corresponding samples that signify good crystallinity and clear lattice fringes. The lattice fringe with interplanar spacing ( $d$ ) of 0.31 nm is indexed to the XRD plane (111) of face-centered cubic structure of  $\text{CeO}_2$ , whereas other fringes could be ascribed to the (111) crystal plane of the

**Fig. 2** The survey (a), Ce 3d (b), Zr 3d (c), and O 1s (d), XPS spectra of Zr doped CeO<sub>2</sub>

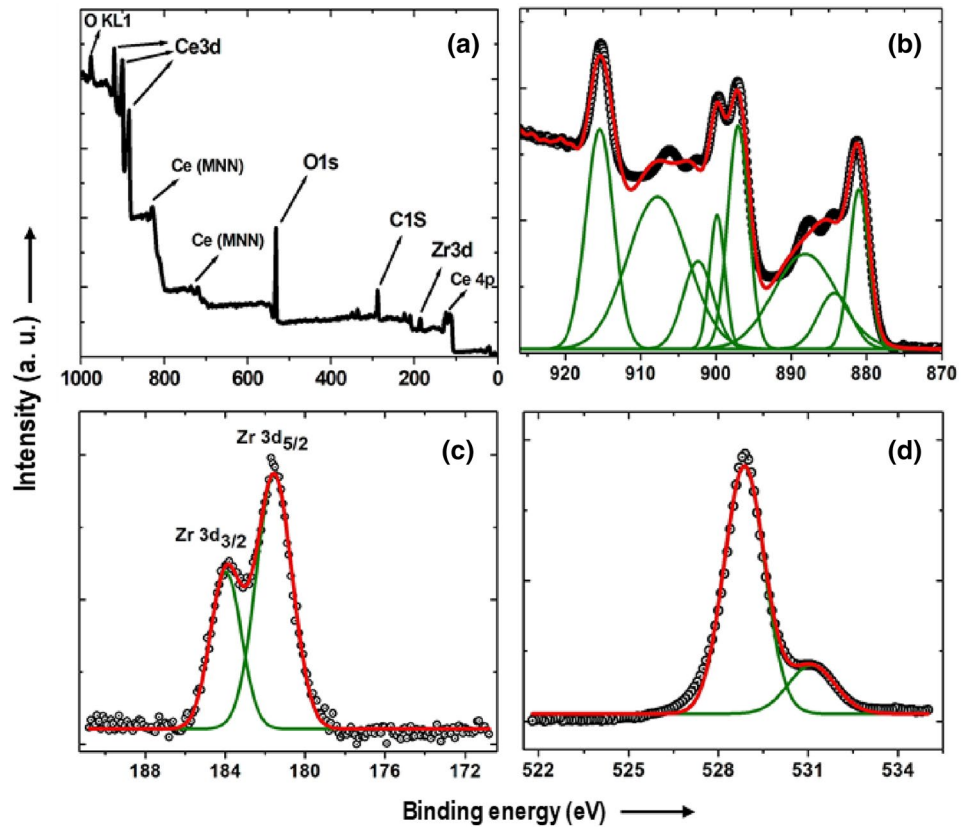
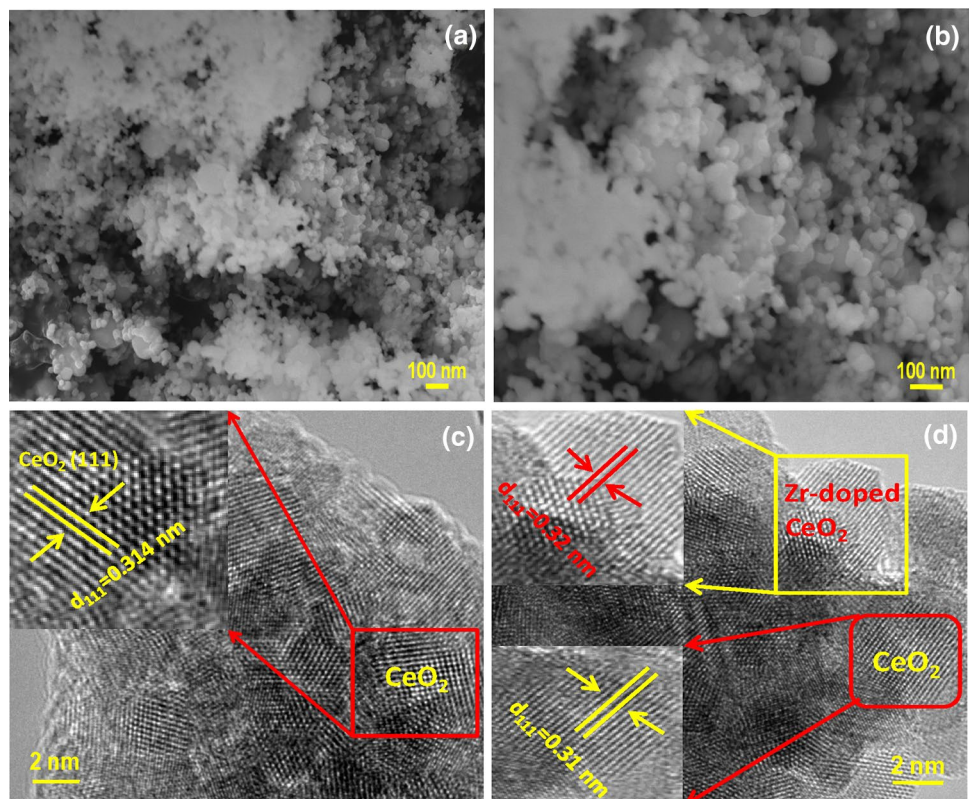


**Fig. 3** a, b SEM, and c, d HRTEM images of the undoped and 10% Zr doped CeO<sub>2</sub> nanoparticles



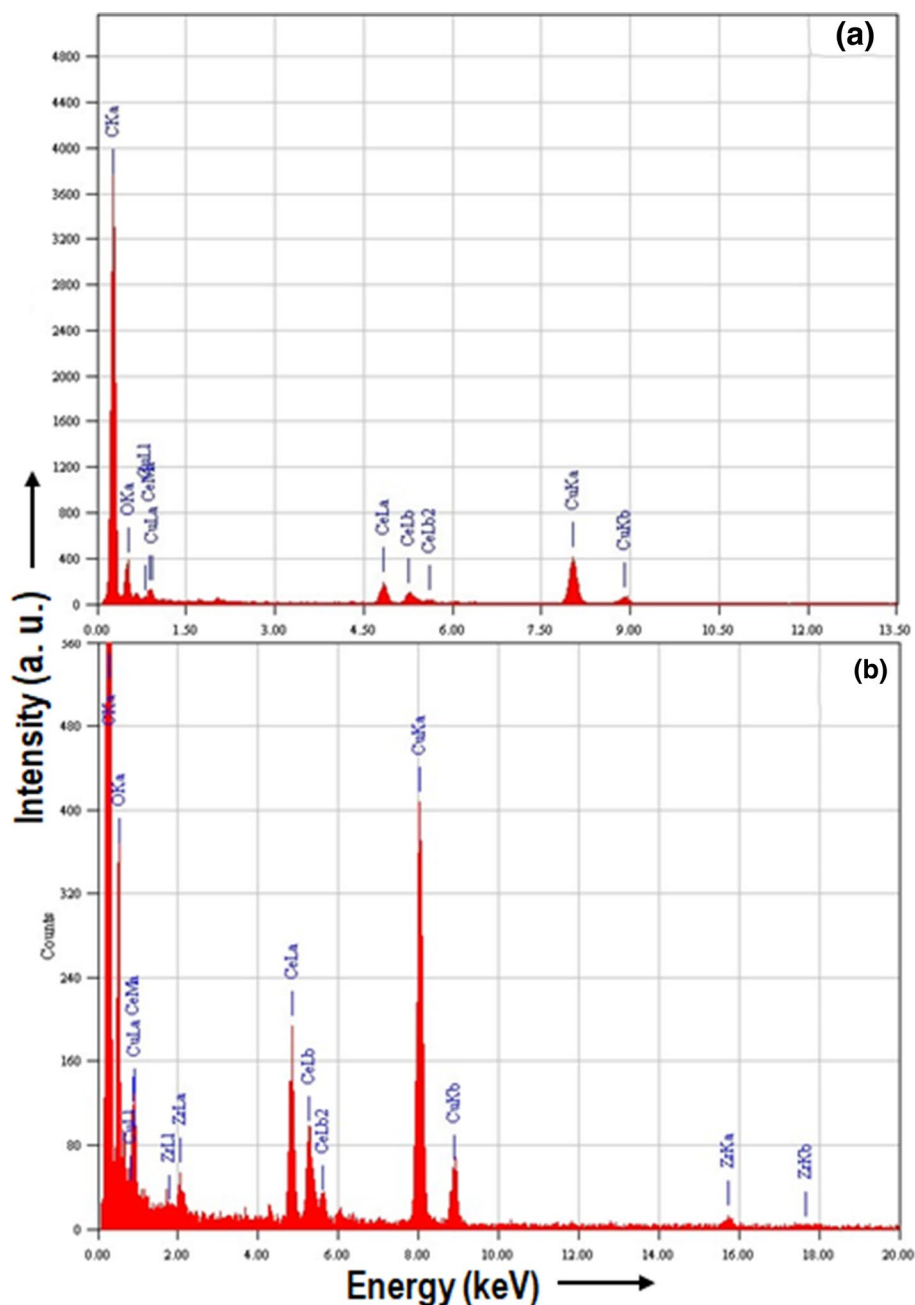


Zr doped nanostructures. The EDS spectra displayed in Fig. 4a, b are used to determine the elemental compositions of the pristine and Zr doped  $\text{CeO}_2$  NPs. It can be seen that only cerium and oxygen as the main species in pure  $\text{CeO}_2$ , while well-defined peaks corresponding to the zirconium, cerium and oxygen elements are present in the Zr doped  $\text{CeO}_2$  NPs that established appropriate existence of the elements in the samples. The elements carbon and copper were detected from the TEM grid used.

### 3.4 FTIR

The vibrational characteristics of the prepared nanoparticles were studied through FTIR spectroscopy analysis in the wavenumbers 400 to 4000  $\text{cm}^{-1}$  and shown in Fig. 5. The IR bands in the range of 400–650  $\text{cm}^{-1}$  are the characteristic peak of ceria appeared in all the samples [42]. The other peaks between 1050 and 1630  $\text{cm}^{-1}$  correspond to the Ce–O stretching vibrations attributed to the adsorbed water on ceria surface [43]. Because of the large surface-to-volume ratio of the nanomaterials, the water molecules are normally absorbed onto the surface from the surrounding environment

**Fig. 4** EDS spectra of **a** undoped and **b** 10% Zr-doped  $\text{CeO}_2$  nanoparticles



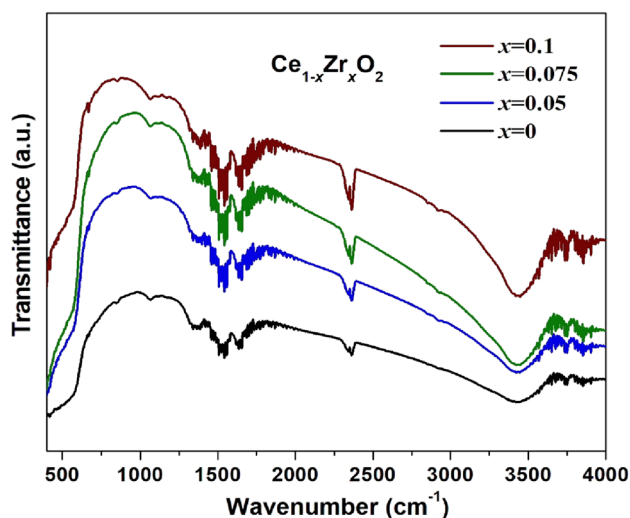


**Fig. 5** FTIR spectra of  $\text{Ce}_{1-x}\text{Zr}_x\text{O}_2$  ( $x=0, 0.05, 0.075$  and  $0.1$ ) samples

[41]. The band at  $2350\text{ cm}^{-1}$  indicates the C–H stretching mode of the methylene groups. However, the absorption peak centered at  $3422\text{ cm}^{-1}$  is associated with the O–H stretching vibrations of water molecules [43].

### 3.5 Raman spectroscopy

It is an excellent technique to get microstructural information of materials. Room temperature Raman spectra of undoped and Zr doped  $\text{CeO}_2$  samples in the wavenumbers  $200$  to  $2500\text{ cm}^{-1}$  are depicted in Fig. 6. A sharp peak at  $465\text{ cm}^{-1}$  appeared in all samples could be associated with

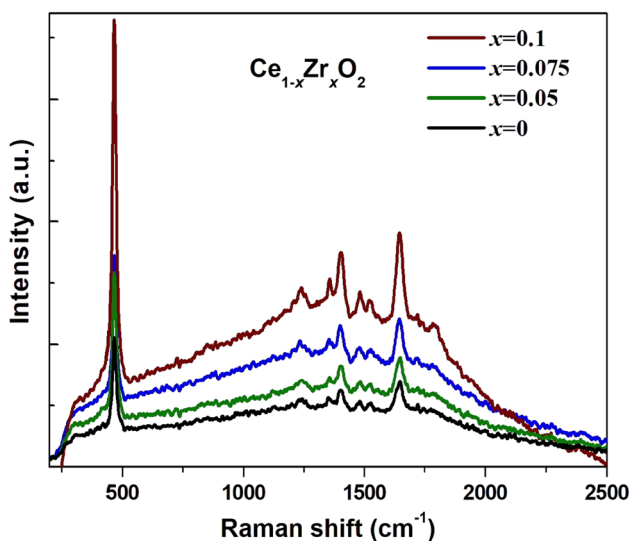


**Fig. 6** Raman scattering spectra of undoped and Zr-doped  $\text{CeO}_2$  nanoparticles

the  $\text{F}_{2g}$  mode of fluorite type cubic structure analogous to the symmetric stretching mode of the oxygen atoms around  $\text{Ce}^{4+}$  ions [44]. The other peaks at  $1237, 1351, 1397, 1481$  and  $1644\text{ cm}^{-1}$  are attributed to the oxygen vacancies generated by the compensation of charge carriers due to the induced defects by the doping ions in  $\text{CeO}_2$  lattice [45]. The outcomes of Raman analysis are consistent with the XRD results.

### 3.6 Optical studies

The influence of doping ion on the optical properties was investigated through UV–vis absorption spectroscopy. Figure 7a shows the UV–vis absorption spectra of pristine and Zr doped  $\text{CeO}_2$  nanoparticles in the wavelengths between  $300$  and  $900\text{ nm}$ . The absorption spectrum of pristine sample shows a broad peak at a wavelength of  $327\text{ nm}$  that signifies slightly blue shift as compared to its bulk counterpart

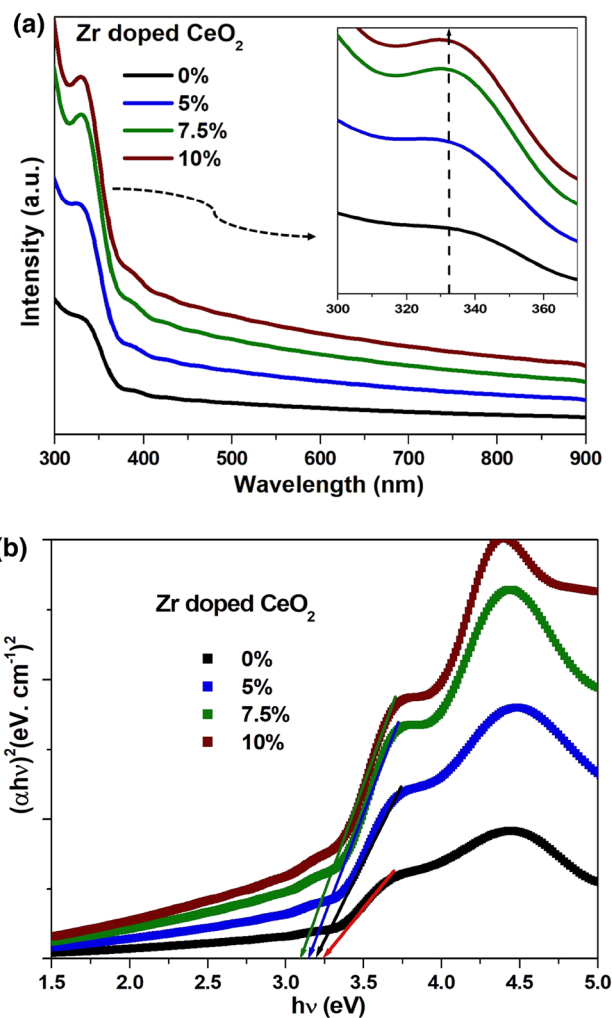


**Fig. 7 a** UV–vis absorption spectra, and **b**  $(\alpha h\nu)^2$  versus photon energy ( $h\nu$ ) plots of  $\text{Ce}_{1-x}\text{Zr}_x\text{O}_2$  ( $x=0, 0.05, 0.075$  and  $0.1$ ) samples

(388 nm) [46]. It indicates the onset of the absorption edge in nanostructures. Further, a red shift in the absorption is observed for the Zr-doped CeO<sub>2</sub> samples. This may be credited to the change in surface to volume ratio of the nanoparticles related to the alteration in the crystallite size or morphology of the nanoparticles. The bandgap ( $E_g$ ) of the samples is evaluated by employing the Tauc's relation given as [47]:

$$(\alpha h\nu)^{1/m} = B(h\nu - E_g)$$

here  $\alpha$  is the absorption coefficient related to the absorbance ( $A$ ) and thickness of the cuvette ( $x$ ) as  $\alpha = 2.303A/x$ , and  $B$  refers a constant that is independent on photon energy. The value of  $m$  depends on the type of optical transition of the semiconductor i.e.  $m = 2$  for direct and  $1/2$  for an indirect transition [48]. The intercept of the linear part of the plot between  $(\alpha h\nu)^2$  and  $h\nu$  is used to calculate the value of  $E_g$  for undoped/doped CeO<sub>2</sub> nanoparticles and illustrated in Fig. 7b. The value of the bandgap is given in Table 1 for all the samples. It indicates that the bandgap of synthesized ceria nanoparticles ( $E_g \sim 3.25$  eV) is slightly higher than its bulk form ( $E_g \sim 3.20$  eV). As particles size decreases, the density of states becomes more quantized and bandgap of the CeO<sub>2</sub> shift towards the higher value. Thus, a blue shift in the absorption band is observed. On the other hand, subsequent doping of Zr ions in CeO<sub>2</sub> reduces the band gap of the system. This may be attributed to the formation of localized states within the bandgap associated with the oxygen vacancies or enhancement in the density of Ce ions [49, 50]. Hence a red shift occurs either ions substitution or interfacial polaron mechanism due to the electron–phonon coupling. This has resulted reduction in the bandgap of the system and theoretically interpreted by the second-order perturbation theory [51].

### 3.7 Photoluminescence spectroscopy

Photoluminescence (PL) is a non-destructive technique generally used for the study of photogenerated electron–hole pairs in semiconductors [52]. Figure 8 shows the room-temperature PL spectra of pristine and Zr-doped CeO<sub>2</sub> nanoparticles excited by a source of wavelength 330 nm. The spectra present emission peaks in the spectral range of 350–650 nm for the pristine and doped samples that exhibit almost identical emission bands, suggested the relative oxygen vacancies in the samples. The emission peaks between 350 and 600 nm are ascribed to the charge transfer transition from Ce 4f to O 2p levels [53]. The doping ion introduces energy levels just below the 4f band of ceria associated with the defects due to the oxygen vacancies. These levels are affected by the temperature and density of defects in material, and hence electron excitation mostly occurs from defects level to O 2p

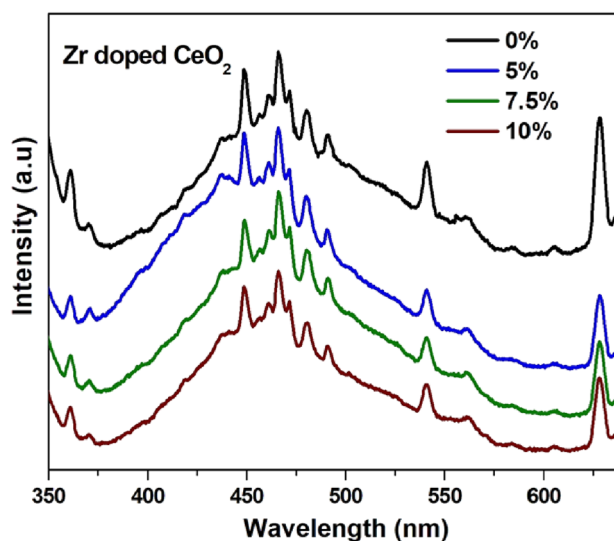


**Fig. 8** PL emission spectra of undoped and Zr doped CeO<sub>2</sub> nanoparticles

level at room temperature [41, 54]. The earlier reports have similar results for CeO<sub>2</sub> nanostructures [55]. In the present study, a considerable improvement in the PL emission is noticed for the undoped CeO<sub>2</sub> in comparison of Zr doped samples that indicates fast recombination rate of electrons and holes in the undoped sample. Therefore, these results confirmed that the doping of Zr ions could delay the recombination rate of photogenerated charge carriers.

### 3.8 Photocatalytic activities

The photocatalytic performance of the synthesized photocatalysts (pristine and Zr doped CeO<sub>2</sub> NPs) were assessed through the deterioration of MB dye under visible light irradiation and shown in Fig. 9. It is noticed that the intensity of characteristic absorption peak of MB dye centred at  $\sim 664$  nm constantly reduces with increase in irradiation time and almost disappeared after 150 min due to degradation of the dye molecules. In order to explore the photocatalytic activities of the samples, the dye concentration as a function of reaction time is studied and displayed in Fig. 9a–e. The variation in concentration of MB dye with irradiation time is shown in Fig. 10 for all studied samples. It is noted that the degradation efficiency of the dye for pure and doped samples is found to be 68.7, 75.8, 80.3 and 92.2% respectively after 150 min irradiation. All Zr doped samples exhibit higher activity as compared to the undoped CeO<sub>2</sub> NPs under visible light irradiation. The enhancement of photocatalytic activity of Zr-doped CeO<sub>2</sub> is attributed to the red shift in the optical adsorption edge on Zr doping in CeO<sub>2</sub> matrix. When Zr is doped in ceria, it behaves as a sensitizer to absorb visible light. The excited electrons of CeO<sub>2</sub> move

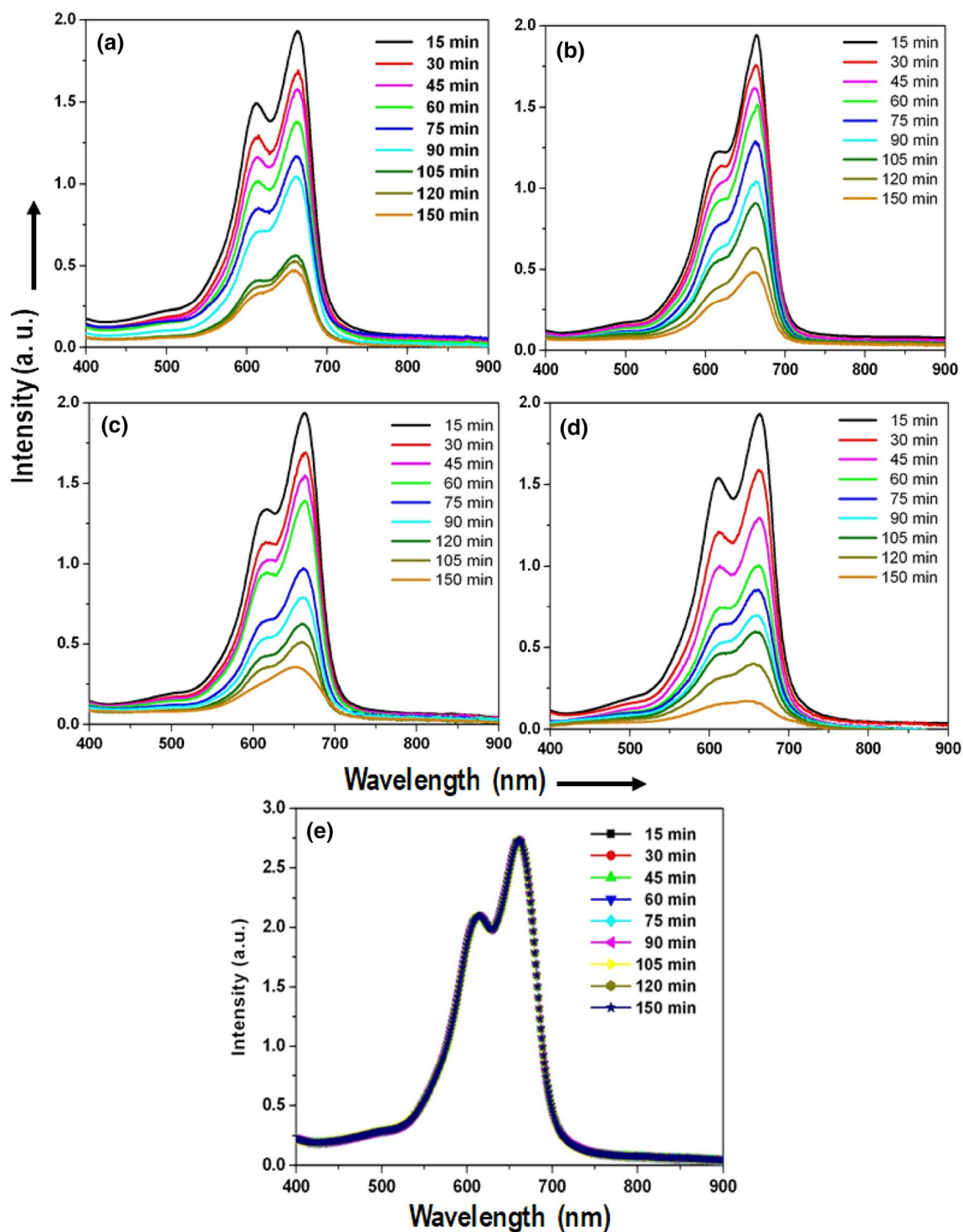


**Fig. 9** UV-Vis absorbance spectra of MB dye at different irradiation times for **a** undoped, **b** 5%, **c** 7.5%, and **d** 10% Zr-doped CeO<sub>2</sub> nanoparticles; **e** in the absence of photocatalyst

to the conduction band of Zr and equal numbers of holes generated in the valence band. In addition, photo-induced electrons transferred from the conduction band to the energy level of dopant ion i.e. Zr<sup>4+</sup> for CeO<sub>2</sub>-Zr system. While the

holes generated in the valence band move to the energy level of -O-Zr-O- for CeO<sub>2</sub>-Zr. This behaviour of charge carriers resulted the higher value of photocatalytic performance for the Zr doped samples than undoped CeO<sub>2</sub>.



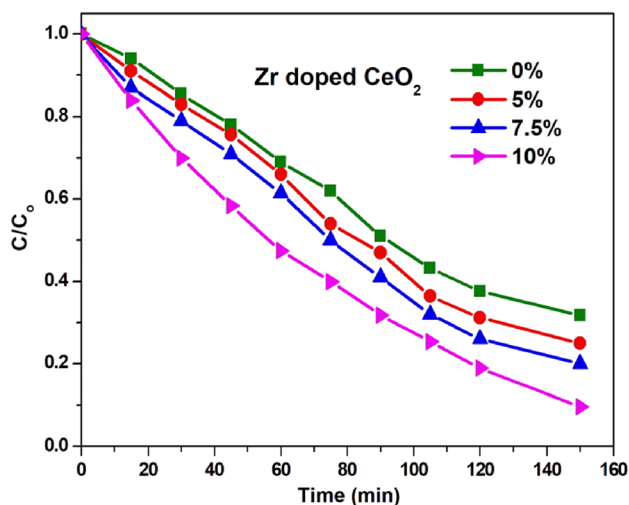


**Fig. 10** Variation in the  $C/C_0$  for the MB dye as a function of irradiation time in the presence of undoped and Zr doped  $CeO_2$  photocatalysts

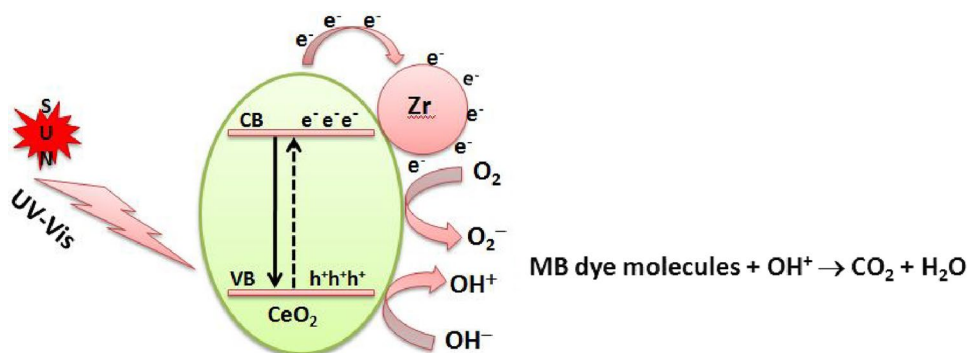
The mechanism for the enhancement in photocatalytic activity of Zr-doped  $CeO_2$  is depicted schematically in Fig. 11 and can be explained as: the slow recombination of electron–hole pairs (as confirmed from PL measurements) resulted in the charge separation at the interface and reach to the photocatalyst surface by diffusion. Generally, recombination of electron–hole pair mainly depends on the PL emission intensity and the lower intensity confirms a decrease in the recombination rate that is beneficial for enhancing photocatalytic activity of catalyst. Another reason of enhancement in the photocatalytic activity can be attributed to the effect of Zr-doping on the optical properties of  $CeO_2$  which help to narrowing the band gap of the matrix and promoting to the improvement of visible light photocatalytic activity of Zr-doped  $CeO_2$ . The possible degradation mechanism of the MB dye through Zr doped  $CeO_2$  already available in literature, however brief description is shown in Fig. 11. When the prepared semiconductor is irradiated by visible light, an electron from valance band (VB) excited to the conduction

band (CB) leaving a hole in valance band. Generally, recombination of these electron–holes reduces the photocatalytic activity of the  $CeO_2$ . But Zr present in the material, trap the electron from CB of  $CeO_2$  that inhibits the electron–hole recombination. It is well established that ‘Zr’ traps the electrons from CB of  $CeO_2$ . Therefore, Zr doping suppresses the electron–hole recombination by the electron trapping [42]. The electrons trapped by Zr produce more number of superoxide radical anions and at the same time VB holes of  $CeO_2$  react with water to produce highly reactive hydroxyl (OH) radical. The superoxide radical anion and hydroxyl radical facilitate the degradation of MB dye.

### 4 Conclusions

The pristine and Zr doped  $CeO_2$  nanoparticles for different concentration of dopant were prepared by a facile simple hydrothermal process. Electron microscopy images revealed uniform and spherical shape of the nanoparticles. HRTEM exhibits crystalline nature of the sample. XPS study confirms that the Zr and Ce ions exist in 4+ state in the doped  $CeO_2$ . Analysis of the optical properties measurements established the presence of oxygen vacancies/defects in the Zr doped  $CeO_2$  samples that make the material suitable for visible light absorption associated with the reduction in band gap. It was observed that the Zr doped nanoparticles have enhanced photocatalytic response as compared to pure  $CeO_2$  for the degradation of MB dye under visible light irradiation. The results predict that the synthesized samples may have promising application water treatment.

**Fig. 11** Schematic illustration of the photocatalytic mechanism of Zr doped  $CeO_2$  system under visible light irradiation



**Acknowledgements** The authors would like to extend their sincere appreciation to the Deanship of Scientific Research at King Saud University for its funding of this research through Group Project No. RGP-1437-023.

## References

- J. Dai, M.L. Bruening, *Nano Lett.* **2**, 497–501 (2002)
- C.T. Campbell, C.H. Peden, *Science* **309**, 713–714 (2005)
- A. Abbasi, D. Ghanbari, M. Salavati-Niasari, M. Hamadani, J. Mater. Sci.: Mater. Electron. **27**, 4800–4809 (2016)
- M.G. Sujana, K.K. Chattopadhyay, S. Anand, *Appl. Surf. Sci.* **254**, 7405–7409 (2008)
- H. Safajou, H. Khojasteh, M. Salavati-Niasari, S. Mortazavi-Derazkola, *J. Colloid Interface Sci.* **498**, 423–432 (2017)
- L. Wang, F. Meng, *Mater. Res. Bull.* **48**, 3492–3498 (2013)
- S. Zinatloo-Ajabshir, M. Salavati-Niasari, M. Hamadani, *RSC Adv.* **5**, 33792 (2015)
- M. Salavati-Niasari, F. Soofivand, A. Sobhani-Nasab, M. Shakouri-Arani, A. Yeganeh Faal, S. Bagheri, *Adv. Powder Technol.* **27**, 2066–2075 (2016)
- H. Yu, Y. Bai, X. Zong, F.Q. Tang, G.Q. Lu, L.H. Wang, *Chem. Commun.* **48**, 7386–7388 (2012)
- P. Singh, N.Q. Minh, *Int. J. Appl. Ceram. Technol.* **1**, 5–15 (2004)
- G. Cheng, J. Xiong, F.J. Stadler, *Powder Technol.* **249**, 89 (2013)
- J. Zhou, L. Zhao, Q. Huang, R. Zhou, X. Li, *Cat. Lett.* **127**, 277–284 (2009)
- J. Zhang, H. Kumagai, K. Yamamura, S. Ohara, S. Takami, et al. *Nano Lett.* **11**, 361–364 (2011)
- R. Bakkiyaraj, G. Bharath, K. Hasini Ramsait, A. Abdel-Wahab, E.H. Alsharaeh, S.M. Chen, M. Balakrishnan, *RSC Adv.* **6**, 51238–51245 (2016)
- V. Matolin, M. Cabala, I. Matolinova, M. Skoda, M. Vaclavu, K.C. Prince, T. Skala, T. Mori, H. Yoshikawa, Y. Yamashita, S. Ueda, K. Kobayashi, *Fuel Cells* **10**, 139–144 (2010)
- P. Jasinski, T. Suzuki, U.H. Anderson, *Sens. Actuators B* **95**(1–3), 73–77 (2003)
- K.S. Brinkman, H. Takamura, H.L. Tuller, T. Iijima, *J. Electrochem. Soc.* **157**, B1852–B1857 (2010)
- D. Wang, Y. Kang, V. Doan-Nguyen, J. Chen, R. Kungas, N.L. Wieder, K. Bakhmutsy, R.J. Gort, C.B. Murray, *Angew. Chem.* **50**, 4378–4381 (2011)
- A. Corma, P. Atienzar, H. Garcia, J.Y. Chane-Ching, *Nat. Mater.* **3**, 394–407 (2004)
- K.S. Hemalatha, K. Rukmani, *RSC Adv.* **6**, 74354–74366 (2016)
- K.S. Ranjith, P. Saravanan, S. Chen, C. Dong, C.L. Chen, S. Chen, K. Asokan, R. Thangavelu, R. Kumar, *J. Phys. Chem. C* **118**, 27039 (2014)
- Y. Liu, C. Wen, Y. Guo, G. Lu, Y. Wang, *J. Phys. Chem. C* **114**, 9889–9897 (2010)
- C.E. Hori, H. Permana, K.Y. Simon Ng, A. Brenner, K. More, K.M. Rahmoeller, D. Belton, *Appl. Catal. B Environ.* **16**, 105–117 (1998)
- M. Adamowska, S. Muller, P. Dacosta, A. Krzton, P. Burg, *Appl. Catal. B Environ.* **74**, 278–289 (2007)
- G. Zhou, P.R. Shah, T. Kim, P. Fornasiero, R. Gorte, *J. Catal. Today* **123**, 86–93 (2007)
- P. Fornasiero, R. Dimonte, G.R. Rao, J. Kaspar, S. Meriani, A. Trovarelli, M. Graziani, *J. Catal.* **151**, 168–177 (1995)
- M. Boaro, C. de Leitenburg, G. Dolcetti, A. Trovarelli, *J. Catal.* **193**, 338–347 (2000)
- P. Periyat, F. Laffir, S.A.M. Tofail, E. Magner, *RSC Adv.* **1**, 1794–1798 (2011)
- P. Venkataswamy, K.N. Rao, D. Jampaiah, B.M. Reddy, *Appl. Catal. B* **162**, 122–132 (2015)
- Z. Wang et al., *Appl. Catal. B* **138–139**, 253–259 (2013)
- W.J. Stark, M. Maciejewski, L. Madler, S.E. Pratsinis, A. Baiker, *J. Catal.* **220**, 35–43 (2003)
- M.A. Wahab, S.S. Physics, Narosa Publishing House, New Delhi, 2nd edn, 2010
- M.A. Majeed Khan, W. Khan, A. Kumar, A.N. Alhazaa, *Mater. Lett.* **219**, 269–272 (2018)
- V.B. Kanattukara, K. Dong-Kyu, P. Dae-Won, *Nanoscale* **2**, 1222–1228 (2010)
- S. Tsunekawa, K. Asami, S. Ito, M. Yashima, T. Sugimoto, *Appl. Surf. Sci.* **252**, 1651–1656 (2005)
- J. Xin Liu, X. Ding, R. Lin, Z. Gao, W.-L. Li, Dai, *Appl. Catal. A* **503**, 117–123 (2015)
- Y. Yu, L. Zhong, J. Ding, W. Cai, Q. Zhong, *RSC Adv.* **5**, 23193–23201 (2015)
- D. Jampaiah, S.J. Ippolito, Y.M. Sabri, B.M. Reddy, S.K. Bhargava, *Catal. Sci. Technol.* **5**, 2913–2924 (2015)
- D. Jampaiah, S.J. Ippolito, Y.M. Sabri, J. Tardio, P.R. Selvakannan, A. Nafady, B.M. Reddy, S.K. Bhargava, *Catal. Sci. Technol.* **6**, 1792–1803 (2016)
- Y.-W. Zhang, R. Si, C.-S. Liao, C.-H. Yan, *J. Phys. Chem. B* **107**, 10159–10167 (2003)
- M.A.M. Khan, W. Khan, M. Ahamed, A.N. Alhazaa, *Sci. Rep.* **7**, 12560 (2017)
- R. Bakkiyaraj, M. Balakrishnan, G. Bharath, N. Ponpandian, *J. Alloy. Compd.* **724**, 555–564 (2017)
- M. Ornatska, E. Sharpe, D. Andreescu, S. Andreescu, *Anal. Chem.* **83**, 4273–4280 (2011)
- J. Lin, L. Li, Y. Huang, W. Zhang, X. Wang, A. Wang, T. Zhang, *J. Phys. Chem. C* **115**, 16509 (2011)
- A. Martnez-Arias et al., *J. Catal.* **240**, 1–7 (2006)
- H. Zhang et al., *Environ. Sci. Technol.* **45**, 3725–3730 (2011)
- S. Kumar, M.A. Majeed Khan, *J. Mater. Sci. Technol.* **29**(12), 1151–1155 (2013)
- M.A. Majeed Khan, M.W. Khan, M. Alhoshan, M.S. AlSalhi, A.S. Aldwayyan, M. Zulfequar, *Mater. Lett.* **64**, 1929–1932 (2010)
- C. Hu, Z. Zhang, H. Liu, P. Gao, Z.L. Wang, *Nanotechnology* **17**, 5983–5987 (2006)
- M.E. Khan, M.M. Khan, M.H. Cho, *Sci. Rep.* **7**, 5928 (2017)
- I. Khan, S. Khan, R. Nongjai, H. Ahmed, W. Khan, *Opt. Mater.* **35**, 1189–1193 (2013)
- M.A. Majeed Khan, S. Kumar, T. Ahamad, A.N. Alhazaa, *J. Alloy. Compd.* **743**, 485–493 (2018)
- S. Kumar, A. Kumar, *Mater. Sci. Eng. B* **223**, 98–108 (2017)
- S.K. Alla, E.V.P. Komarala, R.K. Mandal, N.K. Prasad, *Mater. Chem. Phys.* **182**, 280–286 (2016)
- G. Wang, Q. Mu, T. Chen, Y. Wang, *J. Alloys Compd.* **493**, 202–207 (2010)

**Publisher's Note** Springer Nature remains neutral with regard to jurisdictional claims in published maps and institutional affiliations.